Supplementary Information

Modulating electrolyte solvation for high-performance Aqueous Zinc-Sulfur batteries

Tino S. Thomas, Aayushi Prakash Sinha, Debaprasad Mandal*

Department of Chemistry, Indian Institute of Technology Ropar, Punjab 140001, India

Email: dmandal@iitrpr.ac.in

Materials

Sulfur powder and Zn foil (0.5 mm thickness) were received from Thermo Fischer Scientific whereas, zinc triflate ($Zn(OTf)_2$) was obtained from TCI, N, N-Dimethylacetamide (DMA) was obtained from Spectrochem and zinc iodide (ZnI_2) were procured from Sigma Aldrich. Activated carbon was bought from DTech, Ketjenblack and PVDF were obtained from The Electrode Store. All electrolytes were prepared using de-ionized water with a resistivity of 18 MΩ, and all the above reagents were analytically pure grade and were used without further purification.

Measurements and Characterization

Powder X-ray powder diffraction (PXRD) measurements were conducted using PANalytical X'PERT pro diffractometer using Cu-Kα radiation (λ=0.1542 nm, 20 kV, 20 mA) in the 2θ range from 5 to 80° with a scan speed of 10°/min. FT-IR spectra were recorded with ATR using Bruker Tensor-27, with a zinc selenide window spectrometer ranging from 4000 to 400 cm^{-1}. The various oxidation states and species formed during measurements were recorded using X-ray photoelectron spectroscopy (XPS) via a Thermo Fisher Scientific Escalab Xi^+ spectrometer with monochromatic Al Kα radiation (1486.6 eV) under an ultra-high vacuum (5×10^{-10} mbar pressure). Water contact angle measurements were determined using a Kyowa Contact Angle meter DMe-211 Plus by the sessile water drop method at ambient temperature. Optical images of electrodes before and after cycling were recorded using an Olympus microscope. A LabRAM HR Evolution (Horiba Scientific) was used to record the Raman spectra in the range of 100 cm^{-1} - 500 cm^{-1} using a 532 nm laser as the excitation source. Morphological analysis of materials was done using field emission scanning electron microscopy (FESEM) using JEOL JSM-7610F.

Electrochemical measurements

Sulfur (50 wt.%) was incorporated into activated carbon (50 wt.%) by physical grinding followed by the melt diffusion method under inert conditions at 155 °C for 12 h. The solids obtained were

allowed to cool down to room temperature and denoted as S@AC. The sulfur cathode for all electrochemical measurements was prepared by mixing S@AC, Ketjenblack, and PVDF in a weight ratio of 8:1:1 in N-Methyl-2-pyrrolidone (NMP). The cathodes were dried at 60 °C in a vacuum oven for 12 h to ensure the removal of moisture from the surface. For the Swagelok cell assembly, the mixed slurry was evenly coated on graphite foil of diameter 10 mm with sulfur loading between 1.3-1.5 mg cm^{-2}, zinc foil with a diameter of 10 mm served as an anode, and glass fiber GF-D assembled in between the electrodes served as a separator. Different electrolytes containing 2M $Zn(OTf)_2$ in water (denoted as AZ) were prepared as follows: AZ, AZ/D, AZ/ZnI_2, and AZ/D(x%)/ZnI_2, where x% represents v/v ratio of 20%, 40%, and 60% DMA:water respectively with 0.05 wt.% ZnI_2 added in all the electrolytes. 60 µL electrolytes were used in all battery studies. Linear sweep voltammetry (LSV) and electrochemical impedance (EIS) were carried out using Autolab M204 and Nova 2.1.5 software using glassy carbon as the working electrode. Linear polarization was performed using zinc foil as a working electrode at 1 mV s^{-1} scan rate from -0.3 V to +0.3 V vs OCP while electrochemical impedance spectroscopy (EIS) was recorded from 1 MHz to 0.1 Hz. All batteries were rested overnight before cycling at ambient conditions. The galvanostatic charge-discharge (GCD) profile of Zn//Zn symmetrical cells and Zn/S batteries, cyclic voltammetry, and electrochemical impedance spectroscopy (EIS) were performed using the battery cycler (BCS-810, Biologic) at ambient conditions.

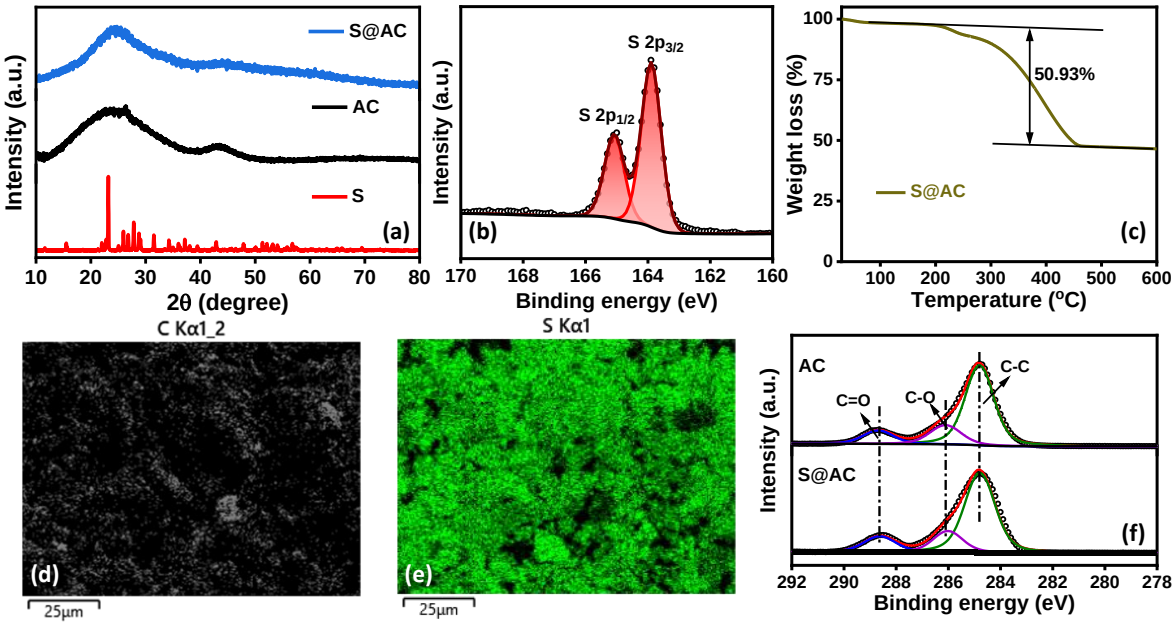

Figure S1. (a) PXRD of pristine S, activated carbon AC, and composite S@AC. (b) Deconvoluted S2p XPS spectra of S@AC. (c) TGA of the S@AC composite. EDS elemental dot mapping of (d) carbon, and (e) sulfur of the S@AC composite. (f) C1s XPS spectra of AC and S@AC.

The conductivity of sulfur was enhanced by incorporating it into the activated carbon matrix wherein sulfur was successfully infused inside the pore of the activated carbon as seen from the powder XRD (Figure S1a). Due to high carbon content, the sulfur lost its long-range ordering in the presence of more nucleation sites in the carbon matrix and thus, the characteristic crystalline peak of sulfur remains absent. Further, X-ray photoelectron spectroscopy of the S@AC composite was carried out to identify the elemental state of the infused sulfur in the carbon matrix. As seen from Figure S1b, the $S2p_{3/2}$ and $S2p_{1/2}$ peaks at 164.2 eV and 165.3 eV respectively confirm the presence of elemental sulfur in its zero-valence state. Moreover, thermogravimetric analysis (TGA) was analyzed and the composite was found to consist of ~51% elemental sulfur (Figure S1c). Elemental dot mapping confirmed homogeneous distribution of sulfur and activated carbon in S@AC composite (Figure S1d, e). To understand the interaction between sulfur and activated carbon after melt diffusion, XPS was recorded. Deconvoluted C1s spectra of AC showed the presence of C-C, C-O and C=O functional groups at 284.8 eV, 286.1 and 288.6 eV, respectively. However, no change in binding energy in C1s spectra for S@AC was observed, implying absence of chemical interaction between sulfur and carbon. This suggests that sulfur is chemisorbed within the pores of AC.

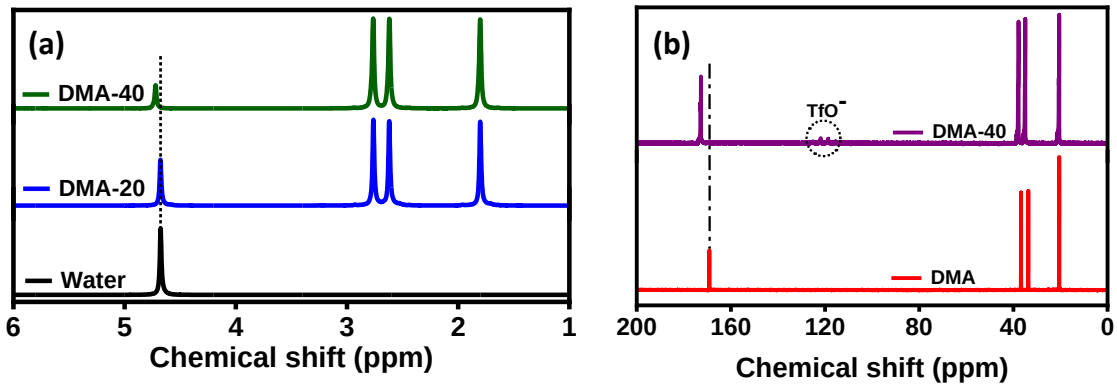

Figure S2. (a) ^{1}H and (b) ^{13}C NMR spectra of different DMA-water mixture in the presence of 2 M $Zn(OTf)_2$.

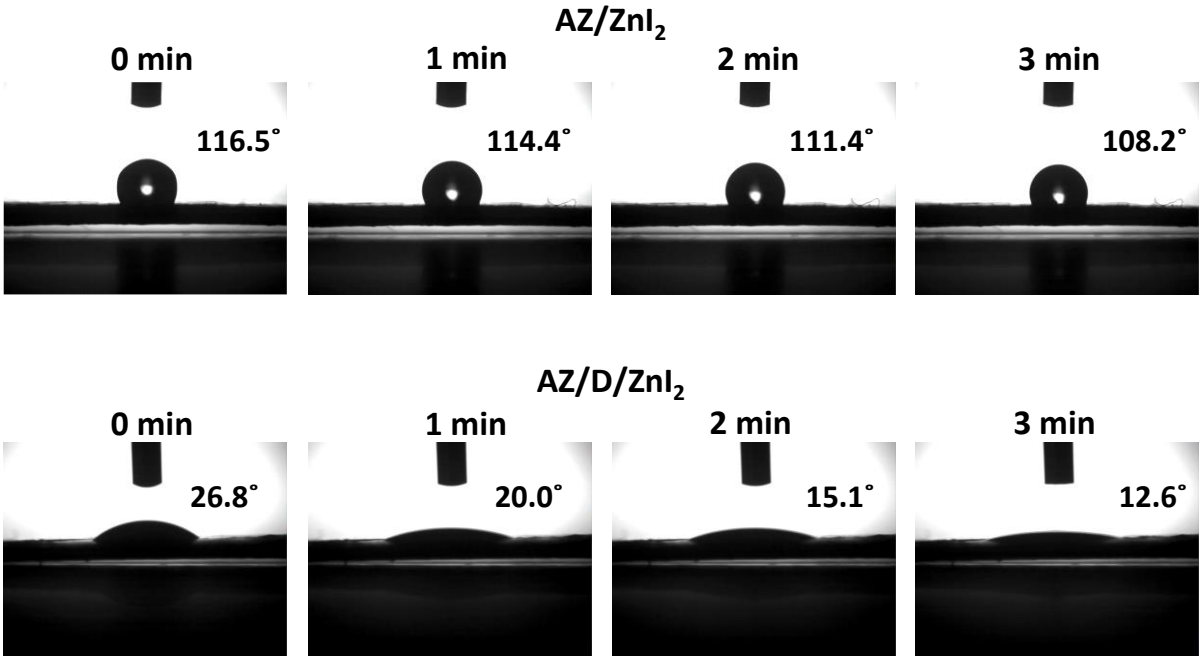

Figure S3. WCA of AZ/ZnI_2 and $AZ/D/ZnI_2$ electrolytes on sulfur cathode.

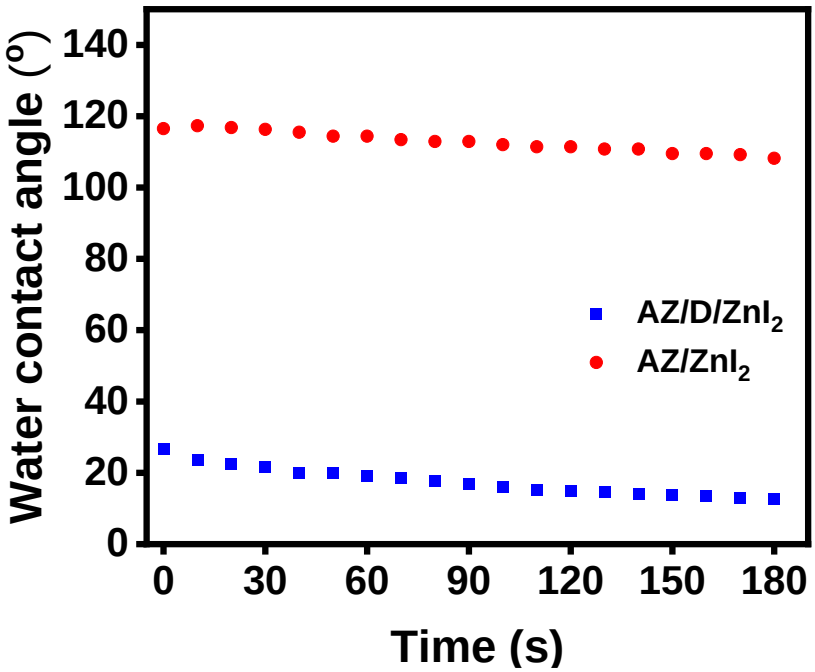

Figure S4. WCA of AZ/ZnI_2 and $AZ/D/ZnI_2$ electrolytes on sulfur cathode with change in time.

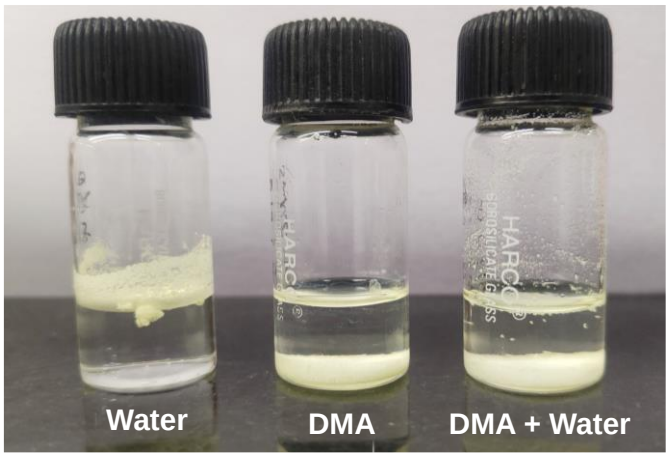

Figure S5. Wettability of sulfur powder in water, DMA, and a mixture of DMA/water (40/60 v/v).

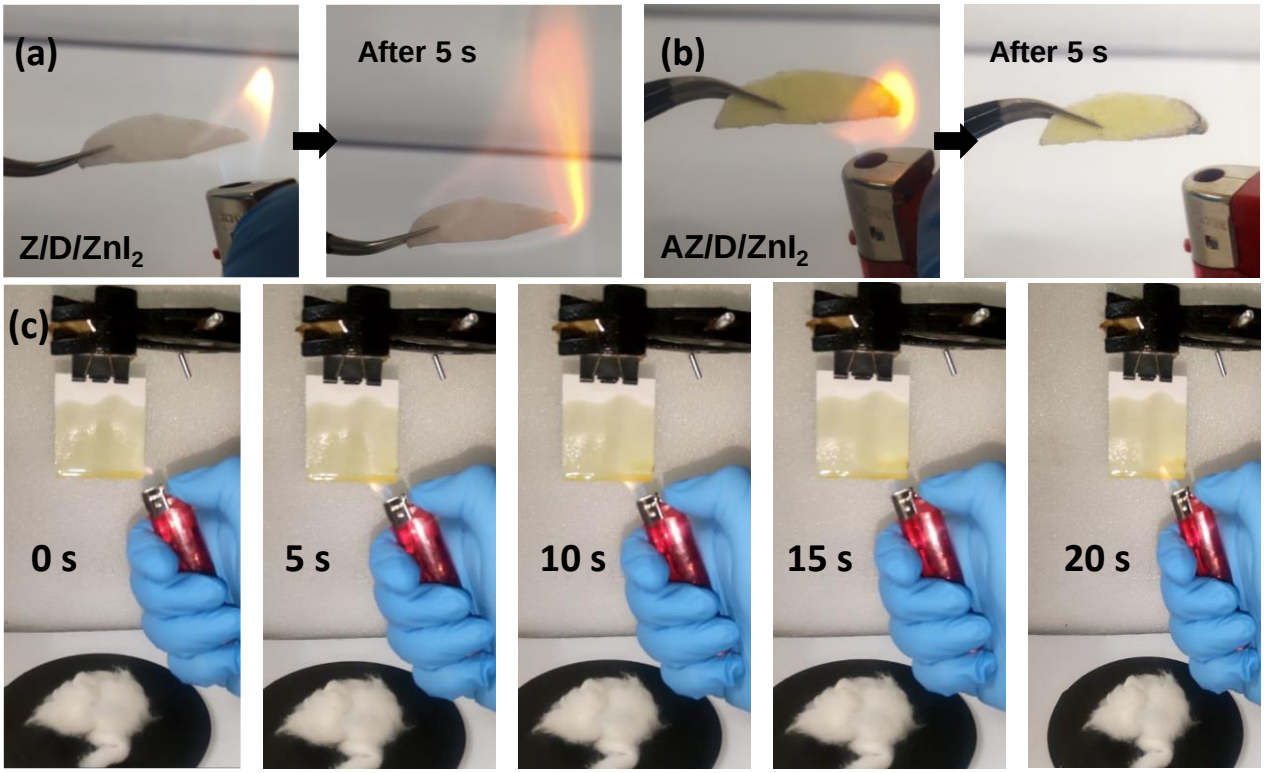

Figure S6. Flammability test of separator soaked in (a) Z/D/ZnI_2 and (b) AZ/D/ZnI_2 electrolytes. (c) Flame resistant UL-94 test of AZ/D/ZnI_2 electrolyte.

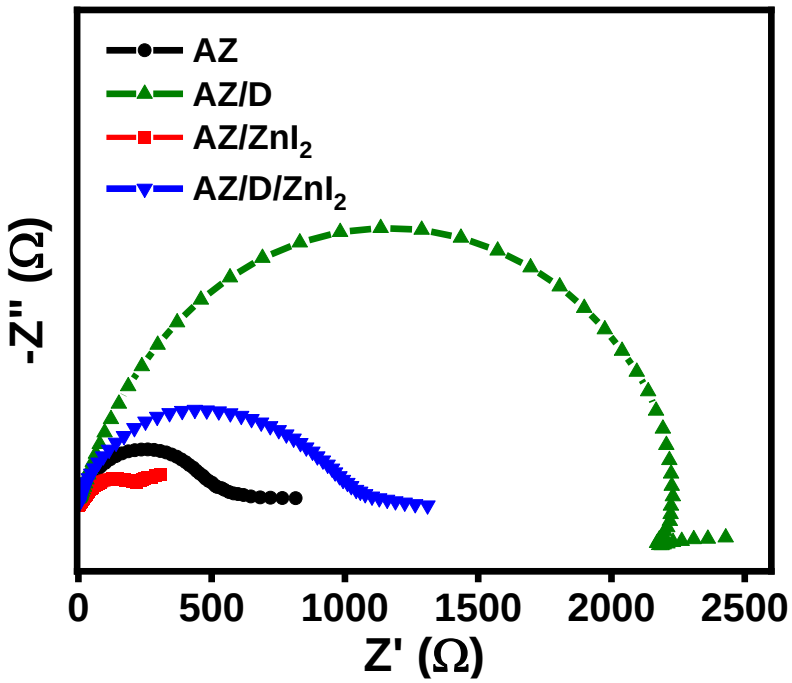

Figure S7. EIS spectra of different electrolytes using Zn as working electrode, Ag/AgCl/3 M KCl as reference electrode and Pt wire as counter electrode.

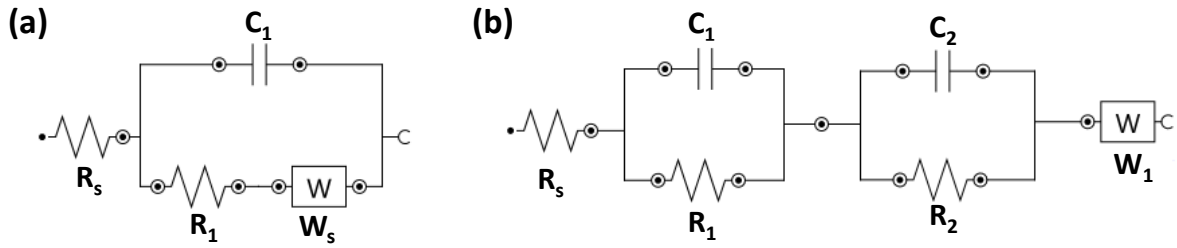

Figure S8. EIS circuit fit of Zn//Zn symmetric cells (after the last cycle at 2 mA cm^{-2}) in (a) AZ/ZnI_2, and (b) $AZ/D/ZnI_2$ electrolyte.

Post cycling of Zn//Zn symmetrical cell in AZ/ZnI_2 electrolyte consists of a Randles circuit corresponding to R_{ct} fitted with a short Warburg element in series. The increase in R_{ct} and addition of W_s after the last cycle as compared to the 10^{th} cycle indicates poor ion diffusion at the interface owing to the generation of corrosion products. This is well supported by FESEM and optical images (Figure 3e and S9a, SI) wherein, a needle-like microstructure appeared due to poor ion diffusion. Furthermore, corrosion products identified as $Zn_xOTf_y(OH)_{2x-y}.nH_2O$ were present on the surface as seen from PXRD (Figure 3d). Furthermore, the post-cycling EIS equivalent circuit in $AZ/D/ZnI_2$ electrolyte is given in Figure S8b (SI). The Nyquist plot reveals two semicircles and a linear feature that corresponds to the resistance of surface film or SEI formed during cycling (R_f), charge transfer resistance (R_{ct}), and Warburg impedance (W), respectively. As the cycling number increased from the 10^{th} to the last cycle, R_f increased as the surface layer grew, however, R_{ct} decreased. The smaller

R_{ct} could be due to the suppression of side reactions, which allowed facile ion movement resulting in an enhanced cycling performance. This observation is well supported from a uniform surface in the optical images and FESEM (Figure 3f and S9b, SI), while the absence of corrosion products was observed from PXRD (Figure 3d).

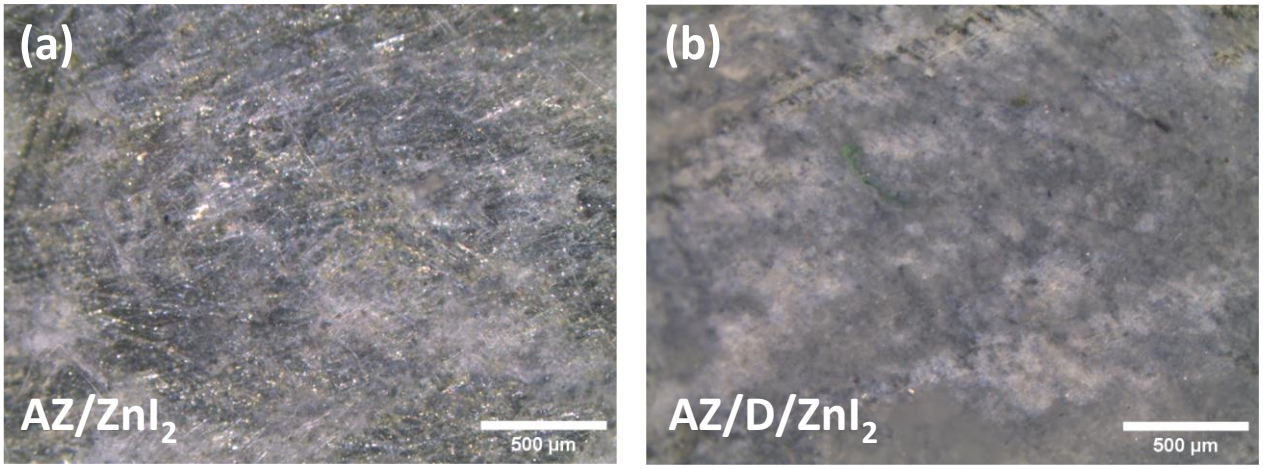

Figure S9. Optical images of Zn electrode after Zn//Zn symmetrical cycling in (a) AZ/ZnI_2, (b) $AZ/D/ZnI_2$ electrolytes.

Optical images show a homogenous and uniform surface of zinc electrode in $AZ/D/ZnI_2$ post cycling indicating stable interface as compared to non-uniform surface seen in AZ/ZnI_2.

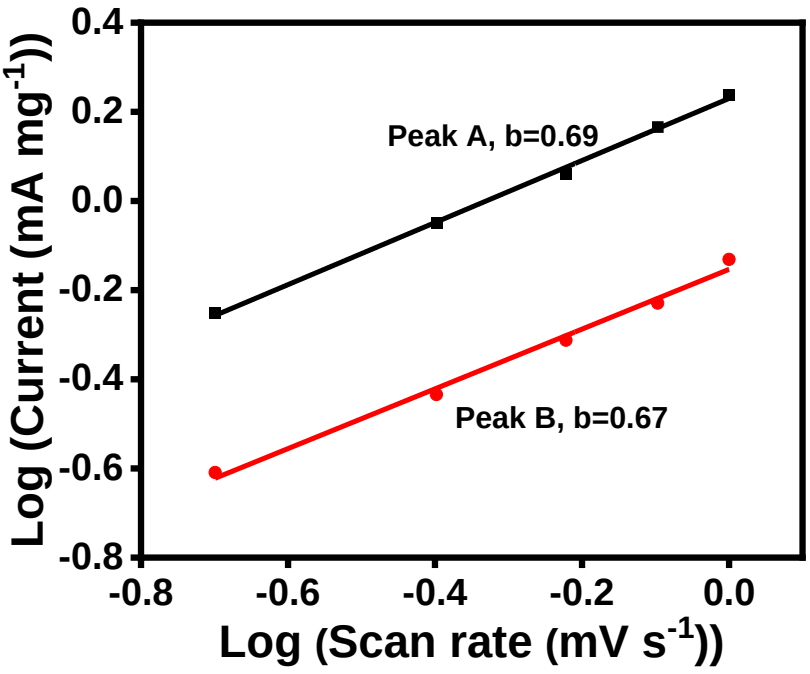

Figure S10. Relationship of log(scan rate) and log(peak current) obtained from cyclic voltammogram at various scan rate of Zn/S battery in $AZ/D/ZnI_2$.

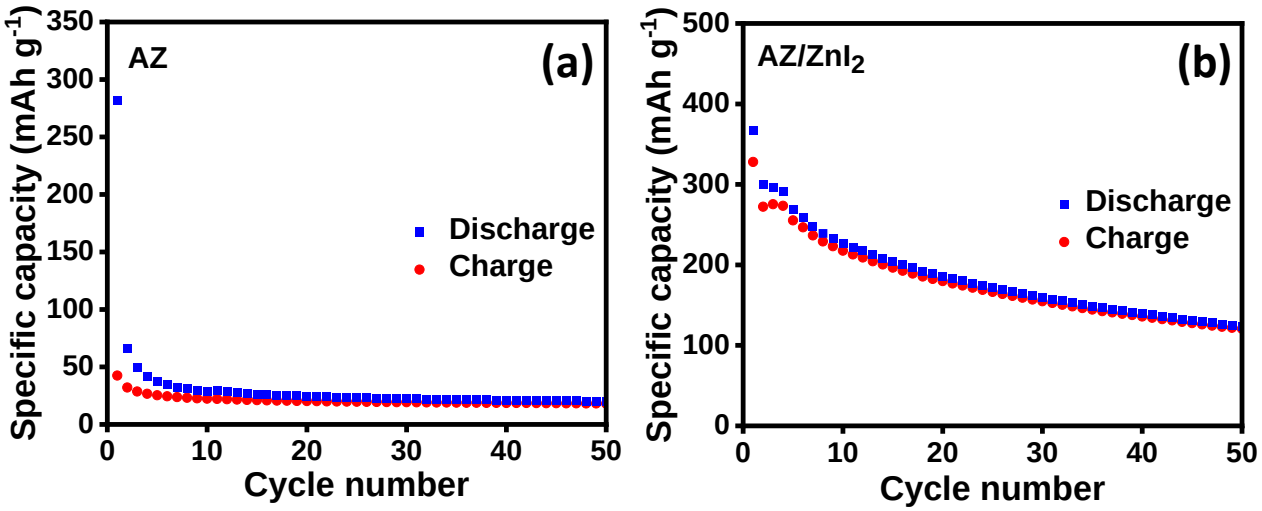

Figure S11. GCD performances of Zn/S batteries operated using (a) AZ, and (b) AZ/ZnI_2 electrolytes for 50 cycles at 1 A. g^{-1}.

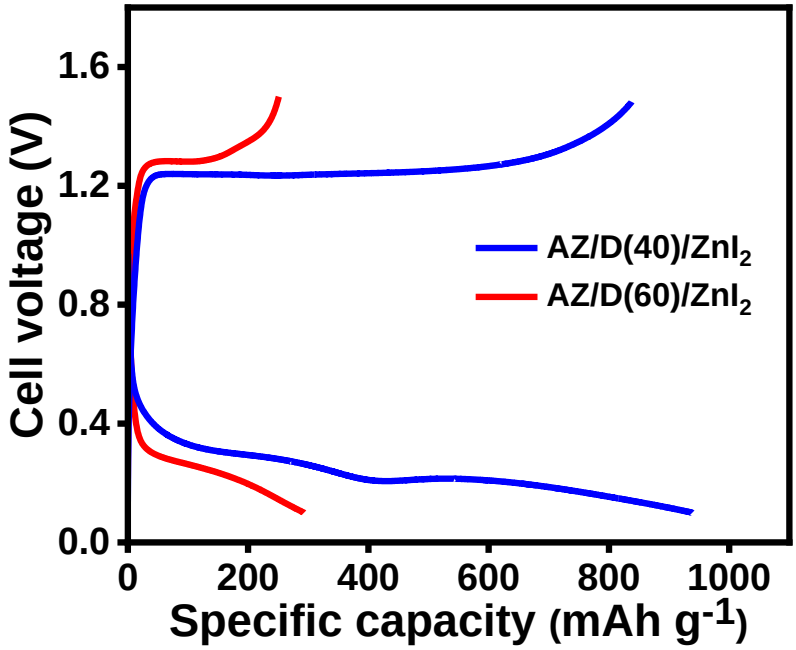

Figure S12. Specific capacity plot of battery operated on AZ/D(40)/ZnI_2 and AZ/D(60)/ZnI_2 electrolytes at 1 A g^{-1}.

Table S1: HER overpotential for different electrolyte with different concentrations of DMA.

Electrolyte	HER overpotential (V)
DMA-0	-0.97
DMA-20	-1.00
DMA-40	-1.08
DMA-60	-1.26 V

Table S2: Solution resistance (R_s) of DMA containing electrolytes.

Electrolyte	R_s (Ω)
DMA-20	36.7
DMA-40	56.3
DMA-60	173.3

Table S3: Performance comparison with reported Zn/S batteries.

Strategy	Anode	Cathode	Electrolyte	Initial capacity (mAh g^{-1})	Cycling Stability	Reference
Electrolyte additive	**Zn foil**	**S@AC**	**2M $Zn(OTf)_2$ + DMA + 0.05 wt.% ZnI_2**	**1453 @0.1 Ag^{-1}**	**72% @5 A g^{-1} (300 cycles)**	**This work**
Electrolyte additive	Zn foil	S@CNTs-50	1M $Zn(CH_3COO)_2$ + 0.05 wt.% I_2	1105 @0.1 Ag^{-1}	85% @1 A g^{-1} (50 cycles)	[1]
Electrolyte additive	Zn foil	CMK-3@S	3M $Zn(OTf)_2$ + 0.1 wt.% I_2	788 @0.2 Ag^{-1}	-	[2]
Electrolyte additive	Zn plate	S@CNTs-50	1m $Zn(CH_3COO)_2$ + PEG-400	1116 @0.1 Ag^{-1}	-	[3]
Electrolyte additive	Zn foil	HCS/S-53.7	2M $Zn(OTf)_2$ + 40% (vol) Tetraglyme +0.15 wt.% I_2	1140 @0.5 Ag^{-1}	70% @4 A g^{-1} (600 cycles)	[4]
Electrolyte additive	Zn foil	S@NPC	2M $Zn(OTf)_2$ + Ethylene glycol + 50 mM ZnI_2	1435 @0.1 Ag^{-1}	70% @3 A g^{-1} (250 cycles)	[5]
Electrolyte additive	Zn foil	ZnS@CF	3M $ZnSO_4$ + 1 wt.% iodinated thiourea (TUI)	1410 @0.1 Ag^{-1}	71% @2A g^{-1} (300 cycles)	[6]
Electrolyte additive	Zn foil	S@KB	1m $Zn(CH_3COO)_2$ + $Me_3PhN^+I^-$	1659 @0.1 Ag^{-1}	60% @3A g^{-1} (100 cycles)	[7]
Electrolyte additive	Zn foil	AJPC/S	1M $Zn(OTf)_2$ + DMC + I_2	1167 @0.1 Ag^{-1}	47.6% @1A g^{-1} (200 cycles)	[8]
Electrolyte	Zn foil	S@C	1M $ZnCl_2$ + D-Zn-Li 5%AN	846 @0.5 Ag^{-1}	21% @1A g^{-1} (400 cycles)	[9]
Electrolyte	Zn foil	CNF-S	$Zn(CH_3COO)_2$-I_2/W-EG	511 @1 Ag^{-1}	39.7% @1A g^{-1} (500 cycles)	[10]
Cathode	Zn foil	S@Fe-PANi	2M $ZnSO_4$	1205 @0.2 Ag^{-1}	54% @1A g^{-1} (200 cycles)	[11]
Cathode	Zn foil	S@FeNC/ NC/CC	2M $ZnSO_4$	1143 @0.2 Ag^{-1}	57.7% @0.5A g^{-1} (300 cycles)	[12]
Cathode	Zn sheet	Te_1S_7/C	1M $ZnSO_4$ + TEGDME	1335 @0.1 Ag^{-1}	91.3% @0.2A g^{-1} (10 cycles)	[13]
Cathode	Zn foil	(poly(Li_2S_6-rDIB)copolymer	1M $Zn(TFSI)_2$ + 21M LiTFSI	1148 @0.3 Ag^{-1}	-	[14]
Anode	powder-Zn/indium (pZn/In)	CMK-3/S	2M $ZnSO_4$ + 20 mM ZnI_2	803 @2C	49% @2C (100 cycles)	[15]

References:

1. W. Li, K. Wang and K. Jiang, *Adv. Sci.*, 2020, **7**, 2000761.
2. Z. Xu, Y. Zhang, W. Gou, M. Liu, Y. Sun, X. Han, W. Sun and C. Li, *Chem. Commun.*, 2022, **58**, 8145-8148.
3. T. Zhou, H. Wan, M. Liu, Q. Wu, Z. Fan and Y. Zhu, *Mater. Today Energy*, 2022, **27**, 101025.
4. M. Yang, Z. Yan, J. Xiao, W. Xin, L. Zhang, H. Peng, Y. Geng, J. Li, Y. Wang, L. Liu and Z. Zhu, *Angew. Chem. Int. Ed.*, 2022, **61**, e202212666.
5. Y. Guo, R. Chua, Y. Chen, Y. Cai, E. J. J. Tang, J. J. N. Lim, T. H. Tran, V. Verma, M. W. Wong and M. Srinivasan, *Small*, 2023, **19**, 2207133.
6. D. Liu, B. He, Y. Zhong, J. Chen, L. Yuan, Z. Li and Y. Huang, *Nano Energy*, 2022, **101**, 107474.
7. W. Wu, S. Wang, L. Lin, H.-Y. Shi and X. Sun, *Energy Environ. Sci.*, 2023, **16**, 4326-4333.
8. D. Patel, A. Dharmesh, Y. Sharma, P. Rani and A. K. Sharma, *Chem. Eng. J.*, 2024, **479**, 147722.
9. M. Cui, J. Fei, F. Mo, H. Lei and Y. Huang, *ACS Appl. Mater. Interfaces*, 2021, **13**, 54981-54989.
10. A. Amiri, R. Sellers, M. Naraghi and A. A. Polycarpou, *ACS Nano*, 2023, **17**, 1217-1228.
11. H. Zhang, Z. Shang, G. Luo, S. Jiao, R. Cao, Q. Chen and K. Lu, *ACS Nano*, 2022, **16**, 7344-7351.
12. W. Zhang, M. Wang, J. Ma, H. Zhang, L. Fu, B. Song, S. Lu and K. Lu, *Adv. Funct. Mater.*, 2023, **33**, 2210899.
13. Y. Zhang, A. Amardeep, Z. Wu, L. Tao, J. Xu, D. J. Freschi and J. Liu, *Adv. Sci.*, 2024, 2308580.
14. Y. Zhao, D. Wang, X. Li, Q. Yang, Y. Guo, F. Mo, Q. Li, C. Peng, H. Li and C. Zhi, *Adv. Mater.*, 2020, **32**, 2003070.
15. J. Li, Z. Cheng, Z. Li and Y. Huang, *Mater. Horiz.*, 2023, **10**, 2436-2444.